Musgrave *et al. eLight* (2026) 6:15
https://doi.org/10.1186/s43593-025-00119-4
elight.springeropen.com

RESEARCH ARTICLE

Open Access

Femtosecond dissipative quadratic soliton mode-locking of cavity-enhanced second-harmonic generation

Jonathan Musgrave[1], Mingming Nie[1,2*] and Shu-Wei Huang[1*]

Abstract

Nonlinear frequency conversion underpins numerous classical and quantum photonics applications but conventionally relies on synchronized femtosecond mode-locked lasers and dispersion-engineered enhancement cavities—an approach that imposes substantial system complexity. To address the challenges, here we report a fundamentally different paradigm: mode-locking of nonlinear frequency conversion enabled by the physics of dissipative quadratic soliton (DQS). We present the operating principle of femtosecond DQS mode-locking and experimentally validate it for the first time in a continuous-wave-pumped doubly resonant second-harmonic generator in free space, yielding bichromatic frequency combs spanning the visible and near-infrared. The observed DQSs exhibit 3 dB optical bandwidths and transform-limited pulse durations of 1.15 THz and 274 fs for the pump and 1.13 THz and 279 fs for the second harmonic. By harnessing phase-matched group-velocity-matched cascaded quadratic nonlinearities, we demonstrate an in-situ tunable effective Kerr nonlinearity that exceeds the intrinsic material response by over three orders of magnitude, enabling femtosecond DQS generation in both free-space and chip-scale cavities across normal and anomalous dispersion regimes. Our results establish a simple, flexible, and scalable approach to nonlinear frequency conversion without the need for synchronized femtosecond mode-locked lasers and expand the reach of soliton-based technologies across diverse cavity platforms and a wide range of challenging wavelengths that are otherwise inaccessible.

1 Introduction

Nonlinear frequency conversion lies at the heart of modern photonics, enabling the generation and manipulation of light at wavelengths inaccessible to conventional sources [1]. By harnessing quadratic nonlinear optical interactions such as second-harmonic generation (SHG), sum- and difference-frequency generation (SFG and DFG), and optical parametric oscillation (OPO), researchers have developed highly tunable light sources critical for applications such as precision metrology, field manipulation, and ultrafast spectroscopy [2–11]. These processes in the quantum regime also serve a foundational role in quantum information science, enabling spectral bridging between disparate systems and facilitating entanglement distribution across quantum networks [12–21].

Traditionally, cavity-enhanced nonlinear frequency conversion has been employed to boost the conversion efficiency by increasing the effective interaction length and intracavity power. This is typically achieved using a dispersion-free resonant cavity synchronously pumped by a femtosecond mode-locked laser (MLL) [2–11].

*Correspondence:
Mingming Nie
mingming.nie@uestc.edu.cn
Shu-Wei Huang
shuwei.huang@colorado.edu
[1] Department of Electrical, Computer and Energy Engineering, University of Colorado Boulder, Boulder, CO 80309, USA
[2] Key Laboratory of Optical Fiber Sensing and Communications (Education Ministry of China), University of Electronic Science and Technology of China, Chengdu 611731, China

However, the reliance on femtosecond MLL and the need for precise synchronization electronics introduce substantial system complexity, increasing the physical footprint and raising the overall cost, posing challenges for widespread adoption.

In this work, we address the challenges of cavity-enhanced nonlinear frequency conversion by demonstrating a fundamentally different paradigm: mode-locking of nonlinear frequency conversion enabled by the physics of dissipative quadratic soliton (DQS) [22–25]. Although DQS was recently demonstrated in a picosecond synchronously pumped optical parametric oscillator [25], spontaneous formation of DQS in continuous-wave (CW) pumped quadratic cavities, *i.e.* DQS mode-locking, has remained elusive until now. Here, we present the operating principle of femtosecond DQS mode-locking and experimentally validate it for the first time in a CW-pumped doubly resonant SHG in free space, yielding bichromatic frequency combs spanning the visible and near-infrared. The observed DQSs exhibit 3 dB optical bandwidths and transform-limited pulse durations of 1.15 THz and 274 fs for the pump and 1.13 THz and 279 fs for the second harmonic.

While DQS and parametrically driven dissipative Kerr soliton (DKS) [26–28] share certain similarities, it is crucial to highlight their fundamentally different mechanisms for balancing dispersion and nonlinearity, as well as the implications of this distinction. In parametrically driven DKS, dispersion engineering is employed to create anomalous dispersion that balances the intrinsically positive material Kerr nonlinearity (MKN). In contrast, DQS relies on an effective Kerr nonlinearity (EKN) arising from cascaded quadratic processes, which not only dominates over MKN but also can be readily tuned via pump detuning (see Results) [24]. The orders-of-magnitude enhancement in EKN enables dissipative soliton formation in free-space cavities, eliminating the need for strongly confining platforms, like fibers or microresonators, and offering a system scalable in both power and energy. Moreover, the dispersive EKN response dynamically changes, reaching its maximum near zero pump phase detuning and reverses sign when detuning is tuned across this point (Fig. 2a-c). This tunability enables EKN to compensate for either normal or anomalous dispersion, offering a wide design space for soliton formation and an *in-situ* method for compensating fabrication defects. Such nonlinearity engineering provides enhanced flexibility in choosing the soliton spectral range and enables the possibility of universal soliton existence. As a demonstration, our free-space doubly resonant enhancement cavity (Fig. 1)—which contains no dispersion engineering elements and is dominated by the normal material dispersion of periodically poled lithium niobate (PPLN)—successfully generates bichromatic DQSs (Fig. 4), made possible by the engineered EKN. Our results establish a new approach for efficient and broadband nonlinear frequency conversion that eliminates the need for synchronized femtosecond MLLs and expands the reach of soliton-based technologies across a wide range of challenging wavelengths that are otherwise inaccessible. DQS offers a simple, flexible, and scalable platform for transformative applications in both classical and quantum photonics [2–21].

2 Results

2.1 Operating principle

Figure 1 illustrates the DQS mode-locking principle of the CW-pumped doubly resonant SHG. As the CW pump—corresponding to the fundamental field—accumulates in the cavity, the second-harmonic (SH) field power increases until it eventually saturates, at which point back-conversion occurs. This cycle of conversion and back-conversion initiates a series of cascaded quadratic nonlinear interactions, including SHG, SFG, DFG, and optical parametric generation (OPG) (top left). Collectively, these processes emulate an effective four-wave mixing interaction, providing the parametric gain and nonlinearity necessary for the spontaneous formation of self-localized DQS (top middle). Notably, in the doubly resonant cavity, the back-conversion can be triggered by pump phase detuning, even under perfect phase matching. Such phase-matched cascaded quadratic nonlinearities (PM-CQNs) enable more efficient nonlinear interactions and allow the effective nonlinearity to be readily controlled through pump phase detuning (top right). This stands in stark contrast to singly resonant cavities, where the effective nonlinearity arises from phase mismatch [24].

Supplementary Information Section II details the theory of the field evolution in the CW-pumped doubly resonant cavity enhanced SHG. Under the good cavity approximation and phase matching condition, the evolution of the coupled pump and SH fields can be described by a single mean-field equation of the pump field

$$t_R\frac{\partial A}{\partial t} = \left(-\alpha_1 - i\delta_1 - i\frac{k_1''L}{2}\frac{\partial^2}{\partial\tau^2}\right)A - (\kappa L)^2 A^*\left[A^2 \otimes \mathcal{F}^{-1}\{J(\Omega)\}\right] + \sqrt{\theta_1}A_{in} \tag{1}$$

Here t is the "slow time" that describes the envelope evolution over successive roundtrips, t_R is the roundtrip time, τ is the "fast time" that depicts the temporal profiles in the retarded time frame, α_1 is the total linear cavity loss for the pump, δ_1 is the pump phase detuning, k_1'' is

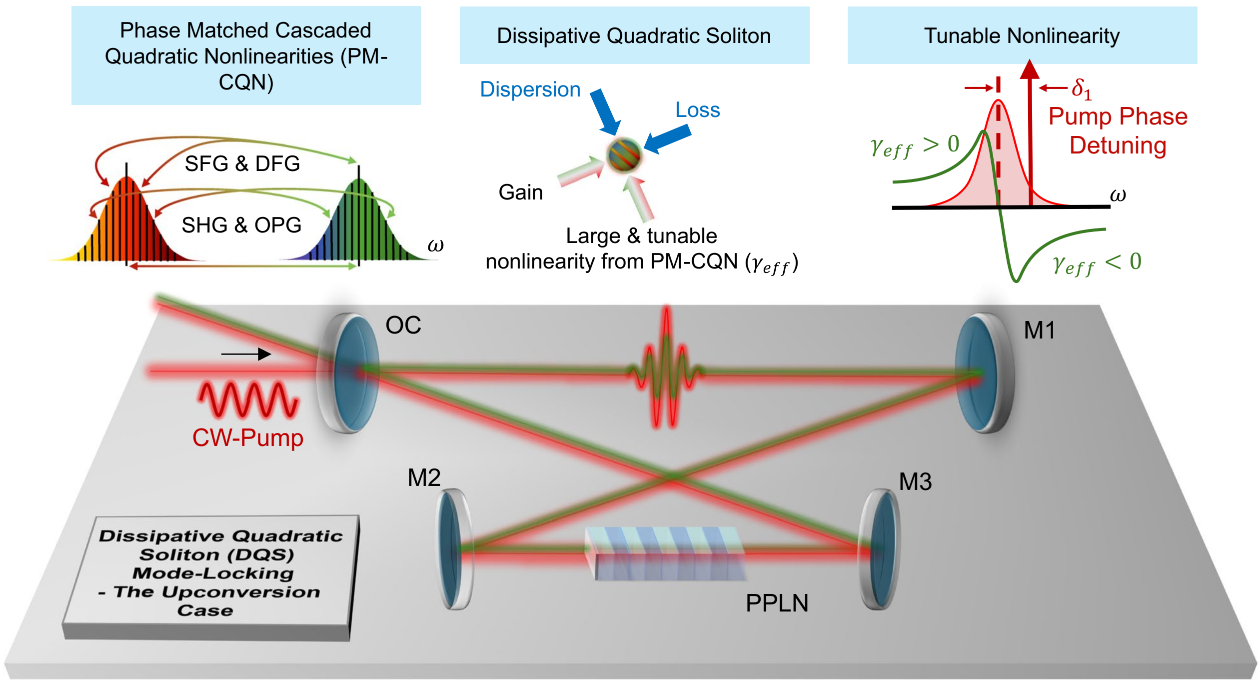

Fig. 1 DQS mode-locked cavity enhanced second harmonic generation. The four-mirror free-space doubly resonant enhancement cavity contains a type-I phase matched PPLN crystal and is pumped by a CW laser with p polarization. OC: 1% output coupler at 1572 nm and 786 nm, M1-M3: mirrors with high reflectivity at 1572 nm and 786 nm. Top left: phase matched cascaded quadratic nonlinearities (PM-CQNs) emulate an effective four-wave mixing that provides parametric gain and nonlinearity. Top middle: DQS is formed due to the double balance among the nonlinearity, dispersion, cavity loss, and parametric gain. Top right: the tunable nonlinearity is readily controlled through pump phase detuning

the pump group velocity dispersion (GVD), L is the nonlinear cavity length, κ is the normalized second-order nonlinear coupling coefficient, $J(\Omega)$ is the nonlinear response function, Ω is the angular frequency around the pump, θ_1 is the pump coupling transmission coefficient, and $|A_{in}|^2$ is the CW pump power. The SH field is dynamically slaved to the pump field and can be explicitly solved from Eq. (1) [29]. As shown in Supplementary Information Section II, $J(\Omega)$ can be decomposed into its real part, $X(\Omega)$, and imaginary part, $Y(\Omega)$, which correspond to the effective two-photon absorption (ETPA) and effective Kerr nonlinearity (EKN), respectively. The two parts can be expressed as

$$X(\Omega) = \left\{\alpha_2\left[1 + \left(\delta_2/\alpha_2 - d_1\Omega - d_2\Omega^2\right)^2\right]\right\}^{-1} \tag{2}$$

$$Y(\Omega) = \left(\delta_2/\alpha_2 - d_1\Omega - d_2\Omega^2\right)X(\Omega) \tag{3}$$

Here, α_2 is the total linear cavity loss for the SH, $d_1 = \Delta k' L/\alpha_2$ is the normalized temporal walk-off between the SH and pump, and $d_2 = k_2'' L/2\alpha_2$ is the normalized group delay dispersion of the SH field. δ_2 is the SH phase detuning. As shown in Supplementary Information Section II, δ_2 is closely related the pump phase detuning δ_1 and the condition $\delta_2 = 2\delta_1$ can be achieved through appropriate tuning of the cavity length and PPLN crystal temperature to achieve perfect phase-matching [27].

Figure 2a plots the dispersive ETPA and EKN as a function of the pump phase detuning δ_1, while Fig. 2b presents the line profiles of ETPA and EKN at $\delta_1 = \pm 5.5\alpha_1$. The parameters are selected to closely reflect the experimental conditions and are provided in Table S1. The case of zero group velocity mismatch (GVM) is considered in the main text and the perturbative effect of non-zero GVM is discussed in Supplementary Information Section III. Two distinct regimes can be identified [24]. The upper zone, where $d_2\delta_1 > 0$, is characterized by two symmetric resonant spectral anomalies while the lower zone, where $d_2\delta_1 < 0$, is characterized by a smooth frequency response with increasing bandwidth at larger $|\delta_1|$. In our cavity, dispersion is primarily governed by the normal material dispersion of PPLN, and thus a clean lower-zone DQS with bichromatic sech^2 spectra is expected when $\delta_1 < 0$ [24].

To draw an intuitive understanding of DQS mode-locking, Eq. (1) can be further simplified by neglecting the dispersion of the ETPA and EKN to

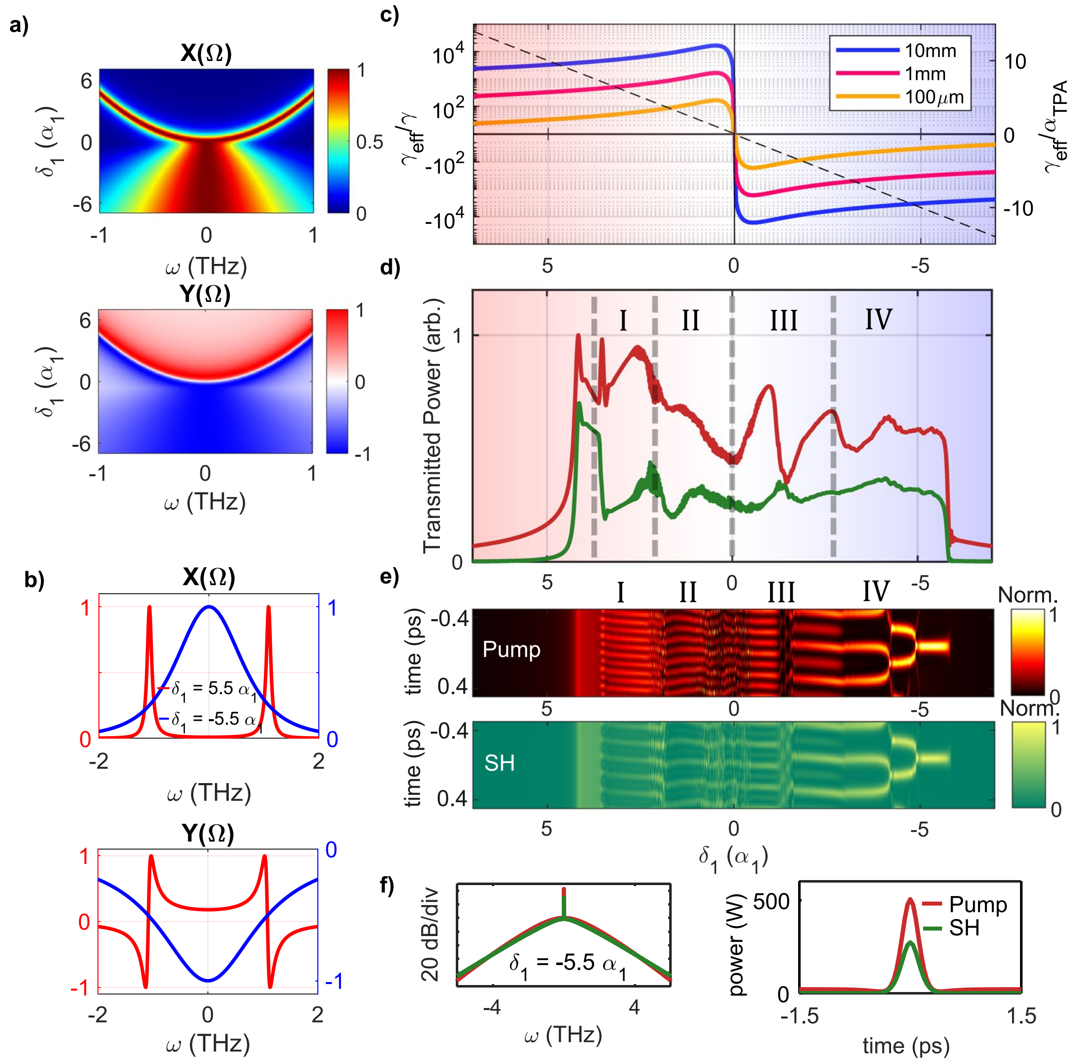

Fig. 2 Numerical simulation of DQS mode-locking – **a** The ETPA (top) and EKN (bottom) as a function of the pump phase detuning, corresponding to the real and imaginary parts of the dispersive nonlinear response function. Both ETPA and EKN are normalized to the peak at each pump phase detuning. **b** The line profiles of ETPA and EKN at $\delta_1 = \pm 5.5\alpha_1$. **c** Ratio of EKN to MKN (left-axis) and EKN to ETPA (right-axis) as a function of pump phase detuning. **d** Simulated cavity transmission as the pump frequency is swept over the cavity resonance from red to blue sides. **e** The corresponding time-domain evolution of the pump and SH fields reveals several distinct dynamical states, which can be categorized into four types. (I) CW state, (II) upper-zone temporal patterns, (III) lower-zone temporal patterns, and (IV) lower-zone DQS states in which the soliton number decreases monotonically as the pump phase detuning becomes more negative. To better visualize the DQSs, a 1-ps time window is selected to crop the simulation results for display purposes. **f** Single DQS optical spectra and pulse shapes when $\delta_1 = -5.5\alpha_1$ showing a 3-dB optical bandwidth and pulse duration of 1.38 THz and 263 fs for the pump and 1.08 THz and 276 fs for the second harmonic

$$t_R \frac{\partial A}{\partial t} = \left(-\alpha_1 - i\delta_1 - i\frac{k_1''L}{2}\frac{\partial^2}{\partial \tau^2}\right)A - \alpha_{\mathrm{TPA}} L|A|^2 A + i\gamma_{eff} L|A|^2 A + \sqrt{\theta_1}A_{\mathrm{in}} \quad (4)$$

Here, $\alpha_{TPA} = X(0) = \alpha_2 L\kappa^2/(4\delta_1^2 + \alpha_2^2)$ is the ETPA coefficient and $\gamma_{eff} = Y(0) = 2\delta_1 L\kappa^2/\left(4\delta_1^2 + \alpha_2^2\right)$ is the EKN coefficient. Figure 2c shows the dependence of α_{TPA} and γ_{eff} on δ_1 for several different crystal lengths. Notably, as δ_1 increases, α_{TPA} approaches zero, and Eq. (4) reduces to the Lugiato–Lefever equation (LLE), which governs conventional DKS dynamics [30]. Due to the large quadratic nonlinearity, the EKN can exceed the intrinsic material Kerr nonlinearity by more than three orders of magnitude in a 10-mm-long type-I phase-matched PPLN crystal. This substantial enhancement significantly lowers the pump power threshold, enabling DQS mode-locking in a free-space cavity. More importantly, the sign of the EKN is governed by the pump phase detuning, allowing it to compensate for either normal or anomalous dispersion and thereby providing a broad design space for DQS formation.

2.2 Numerical simulation of DQS mode-locking

Equation 3 highlights the connection to DKS physics and offers physical insight into the conditions for soliton existence. To further investigate the DQS mode-locking dynamics in a CW-pumped doubly resonant cavity-enhanced SHG system, we numerically solved the coupled Equations S1–S4 provided in Supplementary Section II. The simulation parameters listed in Table S1 closely reflect the actual experimental conditions.

Figure 2d shows the simulated cavity transmission as the pump frequency is swept over the cavity resonance from red to blue sides and Fig. 2e shows the corresponding time-domain evolution of the pump and SH fields. Figure 2d and Fig. 2e reveal several distinct dynamical states, which can be categorized into four types. State I is trivial where the CW pump accumulates in the cavity and the SH field power increases before saturation. Next, the SHG saturation initiates a series of cascaded quadratic nonlinear interactions that results in the transition into state II. Here the pump phase detuning remains positive, and the corresponding upper-zone EKN and ETPA spectral anomalies (Fig. 2a) shape the spontaneous temporal pattern formation [24].

Of note, the PPLN, and consequently the cavity, has normal dispersion at both pump and SH wavelengths. Therefore a lower-zone DQS with bichromatic sech^2 spectra is expected when the pump phase detuning is swept into the negative regime (blue detuning side) [24]. When the pump phase detuning is slightly negative and close to zero, the lower-zone EKN is highly dispersive (Fig. 2a), and the EKN-to-ETPA ratio is low (Fig. 2c). This results in soliton disruption and unstable temporal patterns, characteristic of state III. As the pump frequency is further blue-detuned, the EKN becomes less dispersive, and the EKN-to-ETPA ratio increases, leading to the formation of stable, temporally trapped bichromatic DQSs, corresponding to state IV. In this regime, the number of DQSs decreases monotonically with increasing negative detuning. Ultimately, at a pump phase detuning around $\delta_1 = -5.5\alpha_1$, yields a single DQS is generated with a 3-dB optical bandwidth and pulse duration of 1.38 THz and 263 fs for the pump and 1.08 THz and 276 fs for the second harmonic.

In addition, the perturbative effects of GVM and GVD are discussed in Supplementary Information Sections III and IV, respectively. The GVM between the pump and second harmonic fields acts as the primary perturbation to DQS dynamics, analogous to the role of third-order dispersion in DKS [24]. One strategy to mitigate GVM-induced distortion is to increase the total linear cavity loss, though this comes at the cost of a higher pump power threshold. Supplementary Information Section V then presents simulation results for a cavity with anomalous dispersion, where DQS mode-locking occurs in the positive pump phase detuning regime instead. These findings underscore the tunability of the EKN, which can be tailored to compensate for either normal or anomalous dispersion, thereby providing a broad design space for soliton formation.

2.3 Experimental demonstration of DQS mode-locking

We constructed a CW-pumped, doubly resonant cavity-enhanced SHG system with a free spectral range (FSR) of 380 MHz and a loaded quality factor of 2.70×10^8 (Fig. 1) to experimentally demonstrate DQS generation. The pump wavelength was set to 1572 nm to achieve zero GVM in type-I phase-matched PPLN. While type-I phase matching reduces the effective nonlinear coefficient (d_{eff}) to 2.7 pm/V, it enables birefringence-based tuning that simplifies achieving both phase matching and doubly resonant conditions through precise control of the cavity length and PPLN crystal temperature (with 10 mK resolution) [31]. The GVD at the pump and SH wavelengths are 105 fs^2/mm and 378 fs^2/mm, respectively, which precludes the formation of parametrically driven DKSs. Further details of the experimental setup are provided in the Methods section.

As shown in Fig. 3a, we first investigated the comb dynamics by scanning the pump frequency from the red to blue detuning side at various pump powers. When the pump power was below the SHG saturation threshold of 25 mW, no cascaded quadratic nonlinear processes were observed, as indicated by the absence of sharp features in the cavity transmission of both the pump and SH. When the pump power exceeded the DQS threshold and reached 820 mW, step-like features appeared in the cavity transmission (Fig. 3b), corresponding to distinct dynamical states in agreement with numerical simulations. As anticipated, stable, temporally confined bichromatic DQSs were generated at large negative pump phase detunings. Figure 3c presents the measured pump and SH optical spectra for representative dynamical states. Ultimately, at a pump phase detuning around $\delta_1 = -5\alpha_1$, a single DQS is generated (Fig. 4).

2.4 Characterization of the single DQS state

Figure 4a and b display the measured bichromatic DQS optical spectra, which closely follow the theoretically predicted sech^2 profiles. The pump DQS exhibits a 3-dB optical bandwidth of 1.15 THz, corresponding to a transform-limited 3-dB pulse duration of 274 fs. The SH DQS features a 3-dB optical bandwidth of 1.13 THz, yielding a transform-limited 3-dB pulse duration of 279 fs.

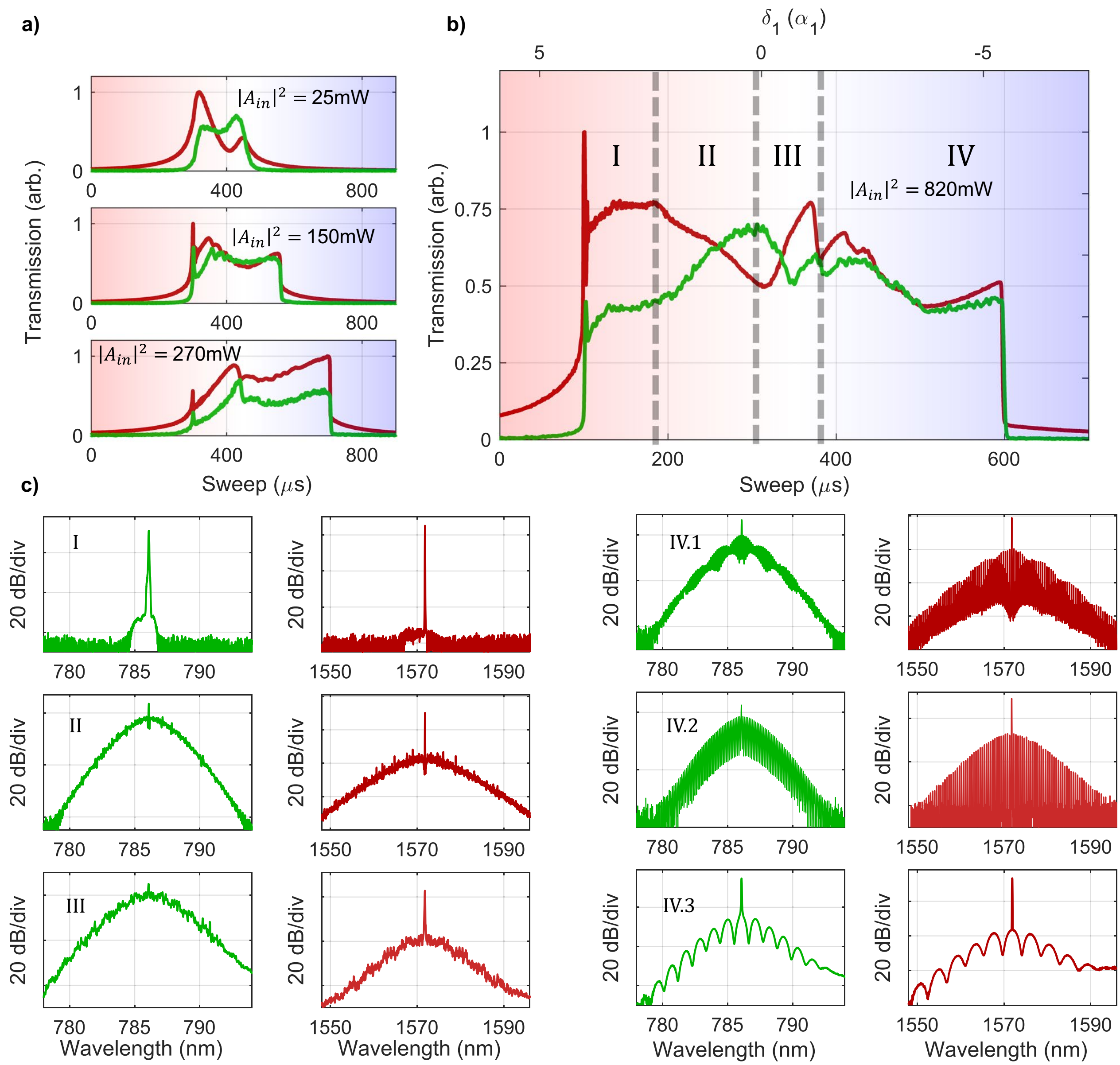

Fig. 3 Experimental demonstration of DQS mode-locking–**a** Cavity transmission of the pump (red) and SH (green) at different pump power as the pump frequency is swept over the cavity resonance from red to blue sides. **b** With an 820-mW pump power, step-like features in the cavity transmission are observed, corresponding to distinct dynamical states that agree with numerical simulations. **c** Optical spectra at the pump and SH wavelengths of different dynamical states. (I) CW state, (II) upper-zone temporal pattern, (III) lower-zone temporal pattern, and (IV) lower-zone DQS states 1 through 3 with different soliton numbers

At the 820-mW CW pump power, pump DQS power of 48 mW and SH DQS power of 23 mW were measured, corresponding to a pump-to-DQS power conversion efficiency of 8.7%. Peak powers of the pump DQS and SH DQS were then estimated to be 500 W and 240 W, respectively. Flat electrical spectra with well-defined beat notes at the fundamental repetition rate (380 MHz) and its harmonics were observed for both the pump and SH DQSs (Fig. 4c and d), consistent with the generation of ultrashort pulses. Additionally, the coherence of the DQSs is verified by the narrow linewidth and high signal-to-noise ratio of the fundamental beat note, as shown in Fig. 4e. The single sideband phase noise spectrum is also included in the Supplementary Information Section VIII.

Finally, Fig. 4f shows the intensity autocorrelation (AC) measurement of the filtered pump DQS that validates the generation of bright femtosecond pulses. Although the 12-nm notch filter effectively suppressed the pump

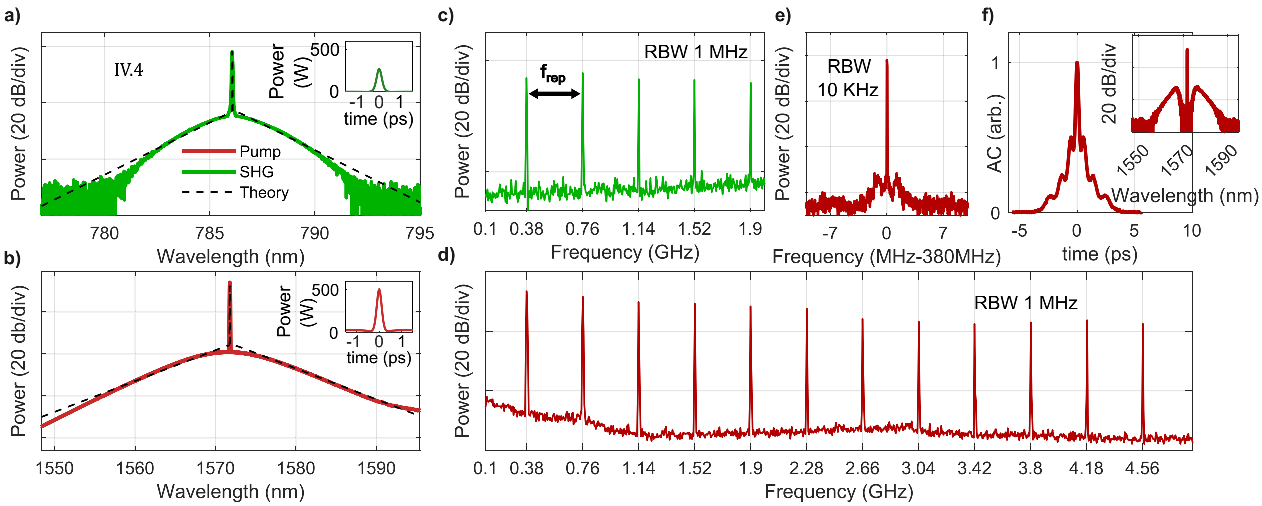

Fig. 4 Characterization of the single DQS state–**a** The measured SH optical spectrum closely matches the theoretically predicted sech^2 profile, exhibiting a 3-dB bandwidth of 1.13 THz. The inset displays the corresponding temporal pulse shape with a 3-dB duration of 279 fs. **b** The measured pump optical spectrum closely matches the theoretically predicted sech^2 profile, exhibiting a 3-dB bandwidth of 1.15 THz. The inset displays the corresponding temporal pulse shape with a 3-dB duration of 274 fs. **c** The measured SH electrical spectrum is flat with clean beat notes spanning the photodetector-limited bandwidth of 2 GHz and taken at a resolution bandwidth (RBW) of 1 MHz. **d** The measured pump electrical spectrum is flat with clean beat notes spanning the photodetector-limited bandwidth of 5 GHz at a RBW of 1 MHz. **e** The fundamental repetition rate beat note at 380 MHz has a resolution-limited linewidth with a signal-to-noise ratio of 50 dB at a RBW of 10 kHz. **f** The intensity autocorrelation (AC) measurement of the filtered pump DQS validates the generation of bright femtosecond pulses. Inset is the pump DQS spectrum after the 12-nm notch filter

for the AC measurement (inset of Fig. 4f), its sharp spectral edges introduced pulse distortion, resulting in pronounced AC tails. Additional details are provided in Supplementary Information Section VI.

3 Discussions

In summary, we have demonstrated femtosecond DQS mode-locking of CW-pumped doubly resonant SHG in free space, yielding bichromatic frequency combs spanning the visible and near-infrared. The observed DQSs exhibit spectral 3 dB optical bandwidths and transform-limited pulse durations of 1.15 THz and 274 fs at 1572 nm and 1.13 THz and 279 fs at 786 nm, respectively. At the 820-mW CW pump power, a pump-to-DQS power conversion efficiency of 8.7% is achieved, with the pump DQS reaching a peak power as high as 500 W. The conversion efficiency of the DQS depends on multiple interrelated pump and cavity parameters that can be carefully engineered to meet specific source requirements. In Supplementary Information Section VII, we present a theoretical analysis of the conversion efficiency for a representative case corresponding to critical coupling at both the FF and SH frequencies under perfect double resonance and phase matching.

By harnessing cascaded quadratic nonlinearities, we realize an EKN that not only surpasses the intrinsic material Kerr nonlinearity by over three orders of magnitude but is also tunable in both magnitude and sign, via pump phase detuning. This *in-situ* engineered nonlinearity is unique in enabling femtosecond DQS generation in both free-space and chip-scale cavities, regardless of whether the dispersion is normal or anomalous. It offers a broad design space for dissipative soliton formation, enhancing flexibility in tailoring the soliton spectral range and supporting the possibility of universal soliton existence. Our results demonstrate a simple, flexible, and scalable approach to nonlinear frequency conversion without the need for synchronized femtosecond mode-locked lasers and expand the reach of soliton-based technologies across diverse cavity platforms and a wide range of challenging wavelengths that are otherwise inaccessible.

The *in-situ* nonlinearity engineering introduces a new degree of freedom in cavity nonlinear optics, with implications extending well beyond nonlinear frequency conversion and frequency comb generation. For example, the approach can compensate the MKN coefficient to maintain high intracavity power while suppressing modulation instability—thereby enhancing the efficiency of entanglement sources for quantum photonic processing [32, 33] and improving the performance of photonic sensors [34–36]. In addition, the reconfigurable EKN coefficient opens new avenues for the development of advanced photonic devices, such as arbitrarily programmable nonlinear photonic circuits for artificial intelligence applications.

4 Methods

4.1 Experimental details

Three of the four mirrors (M1-M3) in the bow-tie cavity are coated with high reflectivity > 99.95% from 1530 to 1580 nm and 765 nm to 790 nm. The output coupler has ~ 1% transmission from 1530 to 1590 nm and 765 nm to 790 nm. The GVM and GVD induced by the mirror coatings are negligible. Both end facets of the 10-mm long 5% MgO-doped PPLN crystal have anti-reflection coating with high transmission at 1572 nm and 786 nm (reflectivity of 0.13% at 1572 nm and 0.09% at 786 nm). The cavity linewidth and quality factor are measured through a frequency-calibrated Mach–Zehnder interferometer (MZI). Figure S1b shows the measured linewidth of 0.7 MHz, correspondingly to a loaded quality factor of ~ 273,000,000. The poling period of the PPLN crystal is 20.6 µm, which is designed for type-I phase matching ($o+o \rightarrow e$) at ~ 1572 nm. The PPLN crystal is placed on a temperature-controlled mount with a resolution of 10 mK and the whole cavity is enclosed in a homemade plastic box to minimize the ambient disturbance.

Fig. S1a is the schematic of the experimental setup. The CW pump laser is an external cavity diode laser (TOPTICA CTL-1550) with a linewidth narrower than 10 kHz over 5 µs. To reliably access and sustain soliton states, the pump laser linewidth must be much narrower than the cavity linewidth (700 kHz). The CW pump is amplified by a 5W EDFA (IPG EAR-LP-SF) and the DQS pump power threshold is as low as 350 mW. To precisely control the pump phase detuning, a frequency-shifted (~ 1 FSR frequency shift from the pump seed laser) CW auxiliary laser is employed to lock to the free-space cavity via the Pound–Drever–Hall (PDH) locking technique. The polarization of the PDH auxiliary laser is matched to that of the CW pump (*p*-polarization), and its power is limited to 10 mW to avoid inducing appreciable nonlinear effects. Furthermore, the CW pump and the frequency-shifted auxiliary laser counter-propagate to minimize crosstalk and enable straightforward separation.

In our current setup, the single DQS state can be maintained for over 10 min, which remains insufficient for many practical applications. The two main limiting factors are (1) the long-term frequency drift of the pump laser (< 5 MHz over 70 s) and (2) cavity-parameter drift caused by inadequate thermal isolation and vibrational shielding from the environment. Nevertheless, reproducing the single DQS state is straightforward and can be reliably achieved by re-scanning the pump frequency. We therefore anticipate that the long-term stability can be substantially improved by incorporating a secondary, slow feedback loop in the PDH locking scheme to compensate for the pump frequency drift, together with a carefully engineered thermal isolation and vibration-suppression system to mitigate cavity drift. Furthermore, the monolithic PPLN cavity [37–40] inherently reduces alignment sensitivity and susceptibility to environmental disturbances, enabling low-noise and robust operation suitable for practical deployment.

Supplementary Information

The online version contains supplementary material available at https://doi.org/10.1186/s43593-025-00119-4.

Supplementary material 1.

Acknowledgements

This work was supported by the Office of Naval Research (N00014-22-1-2224 to S.W.H.) and National Science Foundation (ECCS2048202 to S.W.H.). J.M. acknowledges the support of the Air Force Office of Scientific Research through the NDSEG fellowship.

Author contributions

M.N. and S.W.H. conceived the idea. J.M. and M.N. designed the experiment. J. M. performed the experiment and simulation. J.M., M.N., and S.W.H. conducted the data analysis and wrote the manuscript. S.W.H. led and supervised the whole project. All authors contributed to the discussion and revision of the manuscript.

Funding

Office of Naval Research, N00014-22-1-2224,Shu-Wei Huang,National Science Foundation,ECCS2048202,Shu-Wei Huang,Air Force Office of Scientific Research, Jonathan Musgrave

Data availability

All data generated or analyzed during this study are included in this published article and its supplementary information files. Further source data and codes are available from the corresponding author on reasonable request.

Declarations

Competing interests

J.M., M.N., and S.W.H. are the inventors of a provisional patent application, filed by the University of Colorado Boulder, about the dissipative quadratic soliton (DQS) frequency comb.

Received: 21 August 2025 Revised: 29 December 2025 Accepted: 29 December 2025
Published online: 14 April 2026

References

1. M.M. Fejer, Nonlinear optical frequency conversion. Phys. Today. **47**, 25–32 (1994). https://doi.org/10.1063/1.881430
2. B. Bernhardt, A. Ozawa, P. Jacquet, M. Jacquey, Y. Kobayashi, T. Udem, R. Holzwarth, G. Guelachvili, T.W. Hänsch, N. Picqué, Cavity-enhanced dual-comb spectroscopy. Nat. Photonics. **4**, 55–57 (2010). https://doi.org/10.1038/nphoton.2009.217
3. A. Siddiqui, K.-H. Hong, J. Moses, J. Chen, F.Ö. Ilday, F.X. Kärtner, Demonstration of a cavity-enhanced optical parametric chirped-pulse amplification system. Opt. Lett. **36**, 1206–1208 (2011). https://doi.org/10.1364/OL.36.001206
4. S. Holzberger, N. Lilienfein, H. Carstens, T. Saule, M. Högner, F. Lücking, M. Trubetskov, V. Pervak, T. Eidam, J. Limpert, A. Tünnermann, E. Fill, F. Krausz,

I. Pupeza, Femtosecond enhancement cavities in the nonlinear regime. Phys. Rev. Lett. **115**, 023902 (2015). https://doi.org/10.1103/PhysRevLett.115.023902
5. R.A. Washenfelder, A.R. Attwood, J.M. Flores, K.J. Zarzana, Y. Rudich, S.S. Brown, Broadband cavity-enhanced absorption spectroscopy in the ultraviolet spectral region for measurements of nitrogen dioxide and formaldehyde. Atmos. Meas. Tech. **9**, 41–52 (2016). https://doi.org/10.5194/amt-9-41-2016
6. M.A.R. Reber, Y. Chen, T.K. Allison, Cavity-enhanced ultrafast spectroscopy: ultrafast meets ultrasensitive. Optica **3**, 311–317 (2016). https://doi.org/10.1364/OPTICA.3.000311
7. I. Pupeza, C. Zhang, M. Högner, J. Ye, Extreme-ultraviolet frequency combs for precision metrology and attosecond science. Nat. Photonics. **15**, 175–186 (2021). https://doi.org/10.1038/s41566-020-00741-3
8. A.M. Siddiqui, K.-H. Hong, J. Moses, F.X. Kärtner, Bandwidth extension and conversion efficiency improvements beyond phase matching limitations using cavity-enhanced OPCPA. Opt. Express. **29**, 9907–9926 (2021). https://doi.org/10.1364/OE.415765
9. P. Sulzer, M. Högner, A.-K. Raab, L. Fürst, E. Fill, D. Gerz, C. Hofer, L. Voronina, I. Pupeza, Cavity-enhanced field-resolved spectroscopy. Nat. Photonics. **16**, 692–697 (2022). https://doi.org/10.1038/s41566-022-01057-0
10. T.K. Allison, A. Kunin, G. Schönhense, Cavity-enhanced high-order harmonic generation for high-performance time-resolved photoemission experiments. APL. Photon. **10**, 010906 (2025). https://doi.org/10.1063/5.0244045
11. W.-Q. Fan, S.-Q. Jia, L. Fan, J. Ding, Z.-C. Ren, X.-L. Wang, H.-T. Wang, Cavity-enhanced nonlinear frequency conversion and manipulation of vector fields. APL. Photon. **10**, 036113 (2025). https://doi.org/10.1063/5.0251274
12. H. Takesue, Erasing distinguishability using quantum frequency up-conversion. Phys. Rev. Lett. **101**, 173901 (2008). https://doi.org/10.1103/PhysRevLett.101.173901
13. L. Ma, O. Slattery, X. Tang, Single photon frequency up-conversion and its applications. Phys. Rep. **521**, 69–94 (2012). https://doi.org/10.1016/j.physrep.2012.07.006
14. S.-K. Liao, H.-L. Yong, C. Liu, G.-L. Shentu, D.-D. Li, J. Lin, H. Dai, S.-Q. Zhao, B. Li, J.-Y. Guan, W. Chen, Y.-H. Gong, Y. Li, Z.-H. Lin, G.-S. Pan, J.S. Pelc, M.M. Fejer, W.-Z. Zhang, W.-Y. Liu, J. Yin, J.-G. Ren, X.-B. Wang, Q. Zhang, C.-Z. Peng, J.-W. Pan, Long-distance free-space quantum key distribution in daylight towards inter-satellite communication. Nat. Photonics. **11**, 509–513 (2017). https://doi.org/10.1038/nphoton.2017.116
15. N. Maring, P. Farrera, K. Kutluer, M. Mazzera, G. Heinze, H. de Riedmatten, Photonic quantum state transfer between a cold atomic gas and a crystal. Nature **551**, 485–488 (2017). https://doi.org/10.1038/nature24468
16. L.-Y. Qu, J. Cotler, F. Ma, J.-Y. Guan, M.-Y. Zheng, X. Xie, Y.-A. Chen, Q. Zhang, F. Wilczek, J.-W. Pan, Color erasure detectors enable chromatic interferometry. Phys. Rev. Lett. **123**, 243601 (2019). https://doi.org/10.1103/PhysRevLett.123.243601
17. Y. Yu, F. Ma, X.-Y. Luo, B. Jing, P.-F. Sun, R.-Z. Fang, C.-W. Yang, H. Liu, M.-Y. Zheng, X.-P. Xie, W.-J. Zhang, L.-X. You, Z. Wang, T.-Y. Chen, Q. Zhang, X.-H. Bao, J.-W. Pan, Entanglement of two quantum memories via fibres over dozens of kilometres. Nature **578**, 240–245 (2020). https://doi.org/10.1038/s41586-020-1976-7
18. T. van Leent, M. Bock, R. Garthoff, K. Redeker, W. Zhang, T. Bauer, W. Rosenfeld, C. Becher, H. Weinfurter, Long-distance distribution of atom-photon entanglement at telecom wavelength. Phys. Rev. Lett. **124**, 010510 (2020). https://doi.org/10.1103/PhysRevLett.124.010510
19. X.-Y. Luo, Y. Yu, J.-L. Liu, M.-Y. Zheng, C.-Y. Wang, B. Wang, J. Li, X. Jiang, X.-P. Xie, Q. Zhang, X.-H. Bao, J.-W. Pan, Postselected entanglement between two atomic ensembles separated by 12.5 km. Phys. Rev. Lett. **129**, 050503 (2022). https://doi.org/10.1103/PhysRevLett.129.050503
20. T. van Leent, M. Bock, F. Fertig, R. Garthoff, S. Eppelt, Y. Zhou, P. Malik, M. Seubert, T. Bauer, W. Rosenfeld, W. Zhang, C. Becher, H. Weinfurter, Entangling single atoms over 33 km telecom fibre. Nature **607**, 69–73 (2022). https://doi.org/10.1038/s41586-022-04764-4
21. X. Wang, X. Jiao, B. Wang, Y. Liu, X.-P. Xie, M.-Y. Zheng, Q. Zhang, J.-W. Pan, Quantum frequency conversion and single-photon detection with lithium niobate nanophotonic chips. NPJ. Quantum Inf. **9**, 1–7 (2023). https://doi.org/10.1038/s41534-023-00704-w
22. A.V. Buryak, P.D. Trapani, D.V. Skryabin, S. Trillo, Optical solitons due to quadratic nonlinearities: from basic physics to futuristic applications. Phys. Rep. **370**, 63–235 (2002). https://doi.org/10.1016/S0370-1573(02)00196-5
23. M. Nie, S.-W. Huang, Quadratic soliton mode-locked degenerate optical parametric oscillator. Opt. Lett. **45**, 2311–2314 (2020). https://doi.org/10.1364/OL.389568
24. M. Nie, Y. Xie, B. Li, S.-W. Huang, Photonic frequency microcombs based on dissipative Kerr and quadratic cavity solitons. Prog. Quantum. Electron. **86**, 100437 (2022). https://doi.org/10.1016/j.pquantelec.2022.100437
25. A. Roy, R. Nehra, S. Jahani, L. Ledezma, C. Langrock, M. Fejer, A. Marandi, Temporal walk-off induced dissipative quadratic solitons. Nat. Photonics. **16**, 162–168 (2022). https://doi.org/10.1038/s41566-021-00942-4
26. N. Englebert, F. De Lucia, P. Parra-Rivas, C.M. Arabí, P.-J. Sazio, S.-P. Gorza, F. Leo, Parametrically driven Kerr cavity solitons. Nat. Photonics. **15**, 857–861 (2021). https://doi.org/10.1038/s41566-021-00858-z
27. M. Nie, Y. Xie, S.-W. Huang, Deterministic generation of parametrically driven dissipative Kerr soliton. Nanophotonics **10**, 1691–1699 (2021). https://doi.org/10.1515/nanoph-2020-0642
28. A.W. Bruch, X. Liu, Z. Gong, J.B. Surya, M. Li, C.-L. Zou, H.X. Tang, Pockels soliton microcomb. Nat. Photonics. **15**, 21–27 (2021). https://doi.org/10.1038/s41566-020-00704-8
29. F. Leo, T. Hansson, I. Ricciardi, M. De Rosa, S. Coen, S. Wabnitz, M. Erkintalo, Frequency-comb formation in doubly resonant second-harmonic generation. Phys. Rev. A. **93**, 043831 (2016). https://doi.org/10.1103/PhysRevA.93.043831
30. L.A. Lugiato, F. Prati, M.L. Gorodetsky, T.J. Kippenberg, From the Lugiato-Lefever equation to microresonator-based soliton Kerr frequency combs. Philos. Transact. A Math. Phys. Eng. Sci. **376**, 20180113 (2018). https://doi.org/10.1098/rsta.2018.0113
31. M. Nie, J. Musgrave, S.-W. Huang, Cross-polarized stimulated Brillouin scattering empowered photonics. Nat. Photon. (2024). https://doi.org/10.48550/arXiv.2405.15888
32. I.L. Chuang, Y. Yamamoto, Simple quantum computer. Phys. Rev. A **52**, 3489 (1995). https://doi.org/10.1103/PhysRevA.52.3489
33. M. Heuck, K. Jacobs, D.R. Englund, Controlled-phase gate using dynamically coupled cavities and optical nonlinearities. Phys. Rev. Lett. **124**, 160501 (2020). https://doi.org/10.1103/PhysRevLett.124.160501
34. A.M. Armani, R.P. Kulkarni, S.E. Fraser, R.C. Flagan, K.J. Vahala, Label-free, single-molecule detection with optical microcavities. Science **317**, 783–787 (2007). https://doi.org/10.1126/science.1145002
35. W. Liang, V.S. Ilchenko, A.A. Savchenkov, E. Dale, D. Eliyahu, A.B. Matsko, L. Maleki, Resonant microphotonic gyroscope. Optica **4**, 114–117 (2017). https://doi.org/10.1364/OPTICA.4.000114
36. A. Belsley, E.J. Allen, A. Datta, J.C. Matthews, Advantage of coherent states in ring resonators over any quantum probe single-pass absorption estimation strategy. Phys. Rev. Lett. **128**, 230501 (2022). https://doi.org/10.1103/PhysRevLett.128.230501
37. T. Ikegami, S. Slyusarev, S.I. Ohshima, Long-term, mode-hop-free operation of a continuous-wave, doubly resonant, monolithic optical parametric oscillator. Opt. Commun. **184**, 13–17 (2000). https://doi.org/10.1016/S0030-4018(00)00910-X
38. C.R. Phillips, J.S. Pelc, M.M. Fejer, Continuous wave monolithic quasi-phase-matched optical parametric oscillator in periodically poled lithium niobate. Opt. Lett. **36**, 2973–2975 (2011). https://doi.org/10.1364/OL.36.002973
39. K.P. Jia, X.H. Wang, J. Guo et al., Midinfrared tunable laser with noncritical frequency matching in box resonator geometry. Phys. Rev. Lett. **127**, 213902 (2021). https://doi.org/10.1103/PhysRevLett.127.213902
40. G. Zhao, F. Wang, C. Li, J. Meng, G. Liu, Z. Liu, Single-frequency pump-enhanced monolithic MgO:PPLN optical parametric oscillator and vortex beam generation. Opt. Express. **33**, 8950–8960 (2025). https://doi.org/10.1364/OE.555567